Structural changes in Li_2MnO_3 cathode material for Li-ion batteries

Jatinkumar Rana,[*,†] Marian Stan,[‡] Richard Kloepsch,[‡] Jie Li,[‡] Gerhard Schumacher,[†] Edmund Welter,[¶] Ivo Zizak,[†] John Banhart,[*,†,§] and Martin Winter[‡]

Helmholtz-Zentrum Berlin für Materialien und Energie, Hahn-Meitner-Platz 1, 14109 Berlin, Germany, Institute of Physical Chemistry, MEET Battery Research Centre, University of Muenster, Corrensstrasse 46, 48149 Muenster, Germany, Deutsches Elektronen-Synchrotron, Notkestrasse 85, 22607 Hamburg, Germany, and Technische Universität Berlin, Hardenbergstrasse 36, 10623 Berlin, Germany

E-mail: jatinkumar.rana@helmholtz-berlin.de; banhart@helmholtz-berlin.de

Abstract

Structural changes in Li_2MnO_3 cathode material for rechargeable Li-ion batteries were investigated during the 1^{st} and 33^{rd} cycles by X-ray absorption spectroscopy. It is found that both the participation of oxygen anions in redox processes and Li^+-H^+ exchange play an important role in the electrochemistry of Li_2MnO_3. During activation, oxygen removal from the material along with Li gives rise to the formation of a layered MnO_2-type structure, while the presence of protons in the interslab region, as

---

[*] To whom correspondence should be addressed

[†] Helmholtz-Zentrum Berlin für Materialien und Energie, Hahn-Meitner-Platz 1, 14109 Berlin, Germany

[‡] Institute of Physical Chemistry, MEET Battery Research Centre, University of Muenster, Corrensstrasse 46, 48149 Muenster, Germany

[¶] Deutsches Elektronen-Synchrotron, Notkestrasse 85, 22607 Hamburg, Germany

[§] Technische Universität Berlin, Hardenbergstrasse 36, 10623 Berlin, Germany

a result of electrolyte oxidation and Li^+-H^+ exchange, alters the stacking sequence of oxygen layers from O3-type (ABCABC) to P3-type (ABBCCA). On the other hand, Li re-insertion by exchanging already present protons reverts the stacking sequence of oxygen layers from P3-type back to the original O3-type. The re-lithiated structure closely resembles the parent Li_2MnO_3, except that it contains less Li and O. Mn^{4+} remains electrochemically inactive at all times. Irreversible oxygen release occurs only during activation of the material in the 1^{st} cycle. During subsequent cycles, electrochemical processes seem to involve unusual redox processes of oxygen anions of active material along with the repetitive, irreversible oxidation of electrolyte species. The suggested Li^+-H^+ exchange during each subsequent cycle could involve a repetitive change in the oxygen stacking sequence between O3-type and P3-type. The deteriorating electrochemical performance of Li_2MnO_3 upon cycling could be attributed to the structural degradation caused by repetitive shearing of oxygen layers.

Introduction

The exploration of electrochemical activation in Li_2MnO_3 is important for two main reasons. First, to enhance the fundamental understanding concerning the electrochemistry of Mn^{4+}-containing cathode materials. Second, to obtain the knowledge necessary for designing a possible class of *"Li-rich"* cathodes,[1–9] where Li_2MnO_3 is an important constituting component. Li_2MnO_3 has an O3 structure where close-packed oxygen layers are stacked in an ABCABC sequence. In a layer notation, Li_2MnO_3 can be written as $Li[Li_{1/3}Mn_{2/3}]O_2$ where the interslab octahedral sites are occupied by Li only, while the octahedral sites within the $[Li_{1/3}Mn_{2/3}]O_2$ slabs are occupied by both Li and Mn in a ratio of $1:2$.[10] The fact that in Li_2MnO_3 Mn^{4+} is octahedrally coordinated by O^{2-} led to the initial belief that the material is electrochemically inactive.[11] However, this belief was disproved when a substantial charge could be extracted from the material during an activation process that occurs at 4.5 V vs. Li/Li^+.[12]

Over the past few years, several mechanisms concerning electrochemical activation of Li_2MnO_3 during the 1^{st} charge have been postulated. It has been proposed that Li extraction from Li_2MnO_3 occurs with the simultaneous release of oxygen.[11] Later, it was observed that Li extraction occurs via two competitive processes, namely oxygen removal and Li^+-H^+ exchange.[13–15] The presence of structural defects such as oxygen vacancies also plays an important role in the electrochemical performance of Li_2MnO_3.[16,17] While most of these reports elucidate the structural changes upon Li extraction,[13–15,18] none describes with support by direct experimental evidence from electrochemically treated samples what the structural modifications during Li re-insertion and upon prolonged cycling are.

We study structural modifications in Li_2MnO_3 cathode material during the 1^{st} and 33^{rd} cycles by X-ray absorption spectroscopy (XAS). The elemental selectivity of XAS provides a unique opportunity to probe chemical, electronic and structural changes at and around an absorbing atom. The near-edge region of the absorption spectra is called the X-ray Absorption Near Edge Structure (XANES) and provides qualitative information about the average valence state of absorbing atoms, their local symmetry and electronic configuration. On the other hand, the extended region of the absorption spectra is called the Extended X-ray Absorption Fine Structure (EXAFS) and provides quantitative information about geometrical changes in the vicinity of absorbing atoms. In the present study, the average valence state of Mn and its local symmetry in various Li_2MnO_3 samples are qualitatively discussed in comparison with various manganese reference compounds, while structural changes such as the number of nearest neighbors, interatomic distances and structural disorder are quantified by fitting a theoretical model to the EXAFS data.

Experimental

Li_2MnO_3 was synthesized by a modified Pechini method from acetate precursors.[19] The precursor powders, $Mn(OCOCH_3)_2{\cdot}4H_2O$ and $Li(OCOCH_3){\cdot}H_2O$ were dissolved in an aqueous mixture of ethylene glycol and citric acid (molar ratio 4 : 1). The mole ratio of ethylene glycol and Mn^{2+} was 10 : 1. Dissolution of reagents was completed by heating to 90 °C with constant stirring followed by a temperature increase to 140 °C to promote esterification. Subsequently, the temperature was increased to 180 °C and maintained for 12 h there, during which the polyester formed. Then, the temperature was increased to 250 °C and held for 6 h during which the ethylene glycol dried out and the material caramelized. Calcination at 450 °C for 5 h decomposed the precursors and formed Li_2MnO_3. The calcined Li_2MnO_3 powder was pressed into pellets and annealed at 600 °C for 12 h. The annealed material was characterized for phase purity by X-ray diffraction.

The cathodes for electrochemical characterization were prepared by mixing 80 wt.% active material, 10 wt.% carbon black and 10 wt.% of a solution of polyvinylidene di-fluoride in N-methyl-2-pyrrolidone acting as a binder. The mixture was applied to an aluminum current collector. Electrochemical measurements were carried out in three-electrode Swagelok cells using metallic lithium as a counter and reference electrode. A mixture of ethylene carbonate (EC) and dimethyl carbonate (DMC) (1 : 1 V / V) containing 1 M $LiPF_6$ was used as electrolyte and a glass fiber filter (Whatman GF / D) as separator. The cells were cycled between 2 V and 5 V vs. Li/Li^+ with a constant current density of 4.6 mA/g (i.e. C/50 with 1C = 230 mA/g) during the 1^{st} charge and of 23 mA/g (i.e. C/10) during the subsequent cycles using a Maccor Series 4000 battery testing unit. The open circuit voltage (OCV) of the cell was measured to be $\sim$4.3 V for the charged states and $\sim$2.2 V for the discharged states. The cells were opened in a dry room and cathodes were washed with DMC solution. The active material was scraped off the aluminum current collector and ground using mortar and pestle. The finely ground powder was uniformly applied to the adhesive-coated Kapton tape using a brush. The powder-coated Kapton tape was cut into several pieces which were stacked on top of each other to form a thin, uniform transmission XAS sample.

XAS measurements were carried out in the transmission mode at the Mn K-edge of various Li_2MnO_3 samples. The samples charged and discharged during the 1^{st} cycle were measured at beamline A1 of the Hamburger Synchrotron Radiation Laboratory (HASYLAB), Hamburg, Germany, while those made during the 33^{rd} cycle were measured at beamline KMC-2 of the BESSY-II synchrotron light source, Berlin, Germany. The former is equipped with a Si (111) double crystal monochromator, while the latter has a graded Si-Ge (111) double crystal monochromator. Higher harmonics were rejected by detuning the monochromator such that the intensity of the beam on the sample was 65 % of the maximum possible intensity. Absolute energy calibration of the monochromator was carried out by measuring a reference foil of pure manganese simultaneously with the sample. The intensities of the incident beam and beams transmitted through the sample and the reference foil were measured using gas-filled ionization chambers. The incident beam of 4 mm width and 1 mm height was used at both beamlines. Thus, any structural or compositional inhomogeneities within the individual particle of active material inside the illuminated sample volume were averaged over the entire spectrum. Besides Li_2MnO_3 samples of interest, various manganese reference compounds such as MnO, Mn_2O_3, $LiMn_2O_4$, MnO_2-Pyrolusite and $KMnO_4$ were also measured. All spectra were energy-calibrated with respect to the first peak in the derivative spectrum of pure manganese.

Various data pre-processing operations such as deglitching, averaging the scans, energy calibration, normalization, background subtraction etc.,[20] were performed using the software *ATHENA* of the package *IFEFFIT*.[21] The normalized component of the EXAFS signal was transformed to k-space and the resultant $\chi(k)$ signal was multiplied by k^3 to emphasize the data at high k. The k^3-weighted $\chi(k)$ signal was then Fourier transformed and left uncorrected for phase shift. The theoretical $\chi(k)$ was generated by performing *ab-initio* calculations using the code *FEFF8.2*.[22] The model function was least-square fitted to the data using the software *ARTEMIS* of the package *IFEFFIT* which uses the algorithm *FEFFIT*.[21] The fitting parameters involved a single amplitude reduction factor (S_0^2) and an overall energy parameter (ΔE_0) for each data set. S_0^2 accounts for damping of EXAFS signals as a result of multi-electron excitations or many-body effects.[23–25] S_0^2 is less than 1 and it remains constant for given absorbing atoms over the k-range used for EXAFS analysis.[25] The origin of EXAFS signal in k-space (i.e. $k = 0$) is defined by the threshold energy, E_0. Unfortunately, there is no simple way to determine E_0 from the observed experimental spectrum. Therefore, E_0 is chosen arbitrarily for the experimental data. On the other hand, a model function is calculated by assuming the theoretical absorption threshold for given electronic level of absorbing atom. Thus, in order to align the phase of theoretical $\chi(k)$ with that of the experimental one, ΔE_0 is left as an adjustable parameter in a fit.[25] A fractional change in the bond length (α_{fit}) was refined for each coordination shell such that a change in the bond length ΔR was given by $\Delta R = \alpha_{fit} \times R_{theory}$. Each coordination shell was assigned a separate mean-squared relative displacement parameter (σ^2) depending on the type of atoms it contained and its mean distance from the central absorber. The parameters for multiple scattering paths were constrained in terms of those of corresponding single scattering paths.[26] Various statistical parameters such as χ^2, reduced chi-square (χ^2_ν) and the *R*-factor were used to assess the quality of an EXAFS fit. However, since χ^2 and χ^2_ν are evaluated based on measurement uncertainties and *FEFFIT* poorly estimates the true measurement uncertainties,[26–28] both these parameters do not reflect the true quality of the fit. Nevertheless, both χ^2 and χ^2_ν were used to assess which model fits best the data. The statistical quality of the fit was given by its R-factor which is independent of measurement uncertainties.[26–28] A fit with an R-factor less than 0.02 (i.e. 98 % agreement between data and theory) is considered to be a good fit.[26–28]

Results

As shown in Figure 1a, the cell delivered a specific capacity of 388 mAh/g when charged to 5 V and of 200 mAh/g when discharged to 2 V with a 1^{st} cycle efficiency of ~ 50 % (Figure 1b). The long plateau above 4.5 V vs. Li/Li^+ during the 1^{st} charge that delivers most of the capacity is a characteristic of Li_2MnO_3 [13–15,18,29] and Li_2MnO_3-containing cathode materials.[1–9] The capacity delivered during the 1^{st} charge (i.e. activation) depends on the rate at which the cell is charged. However, the capacity during subsequent cycles is independent of the rate. Therefore, the cell was first-charged to 5 V using C/50, while subsequent cycling was carried out at C/10. As shown in Figure 1b, the electrochemical performance of Li_2MnO_3 degrades upon cycling. During the 33^{rd} cycle, the cell delivers a specific capacity of ~ 110 mAh/g both during charge and discharge, which is just ~ 55 % of that of the 1^{st} discharge.

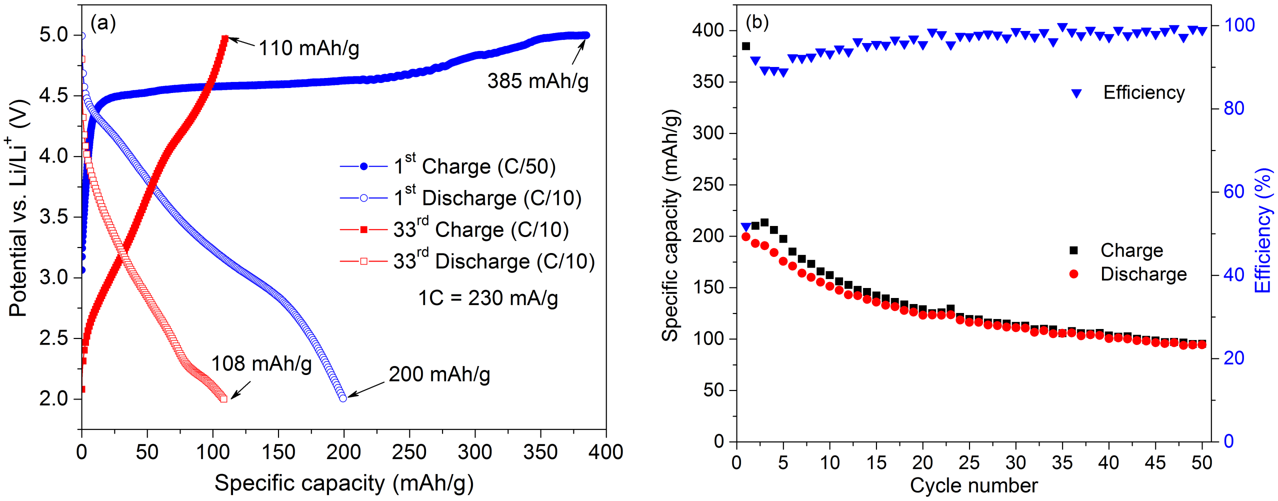

Figure 1: (a) Charge-discharge profiles of Li_2MnO_3 when cycled between 2.0 V and 5.0 V during the 1^{st} and 33^{rd} cycles and (b) Charge-discharge capacities obtained during each cycle along with electrochemical efficiency.

XANES

As shown in Figure 2a, the absorption edge is characterized by a variety of edge-features such as, (1) an absorption threshold (or the first peak in the derivative spectrum, not shown), (2) a $1s\rightarrow 3d$ transition, corresponding to the pre-edge peak, (3) the main edge, corresponding to the vertically rising portion of the edge (or the second peak in the derivative spectrum, not shown) and (4) a $1s\rightarrow 4p$ transition, corresponding to the maximum of the vertically rising portion of the edge.[30] A relative shift in the position of these features, often called a chemical shift, provides an empirical mean for the estimation of the average valence state of the central absorbing atom. The inset in Figure 2a shows an enlarged pre-edge region of these spectra. In order to enhance the visibility of the pre-edge peaks of other reference compounds, the intense pre-edge peak of $KMnO_4$ is omitted from the inset. The pre-edge regions of MnO, MnO_2 and $KMnO_4$ are characterized by a single $1s\rightarrow 3d$ peak, while for Mn_2O_3 this peak is split into two, poorly resolved t_{2g} and e_g peaks. For $LiMn_2O_4$, this peak splitting is better resolved. The intensity of the pre-edge peak is minimum for MnO, intermediate for MnO_2 and maximum for $KMnO_4$.

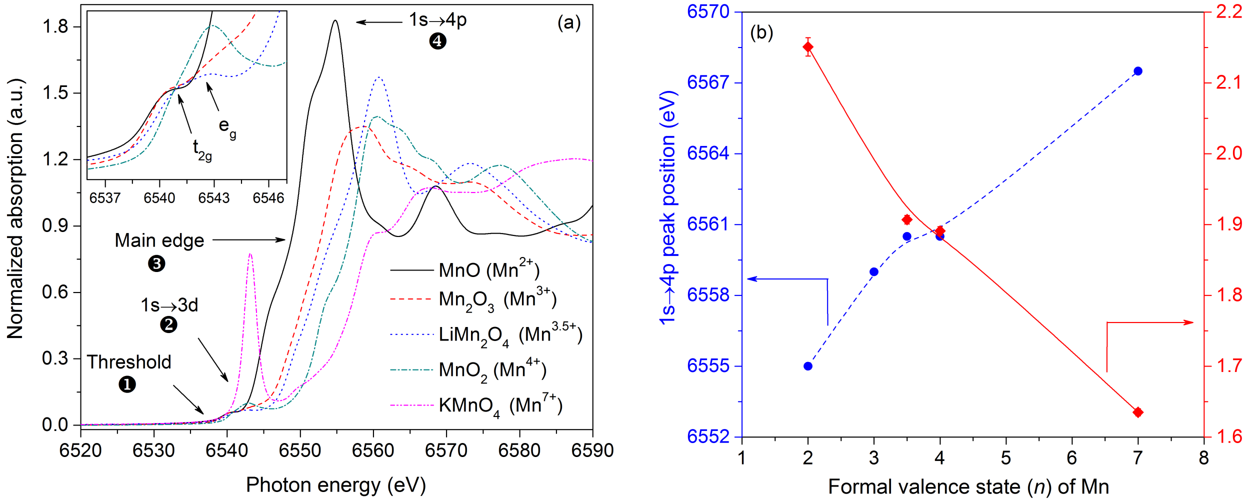

Figure 2: (a) Normalized absorption spectra for various manganese reference compounds with the inset showing an enlarged pre-edge region of four compounds and (b) Variation in the position of the $1s\rightarrow 4p$ peak (dashed blue line) and the average metal-ligand bond length (solid red line) for these compounds.

Inner *d*-orbitals are more tightly bound and, therefore, less sensitive to chemical changes than loosely bound outer *p*-orbitals. Thus, chemical shifts observed at the position of the $1s\rightarrow 4p$ peak are more pronounced than those observed at any other features.[30,31] As a result, chemical shifts are interpreted in terms of the position of the $1s\rightarrow 4p$ peak. Figure 2b shows that with increasing formal valence state of Mn the position of this peak moves to higher energy and the average metal-ligand bond length decreases. The reported values of bond lengths are obtained by fitting the EXAFS data of individual reference compounds (refer to Figure S1 and table S1 in SI.)

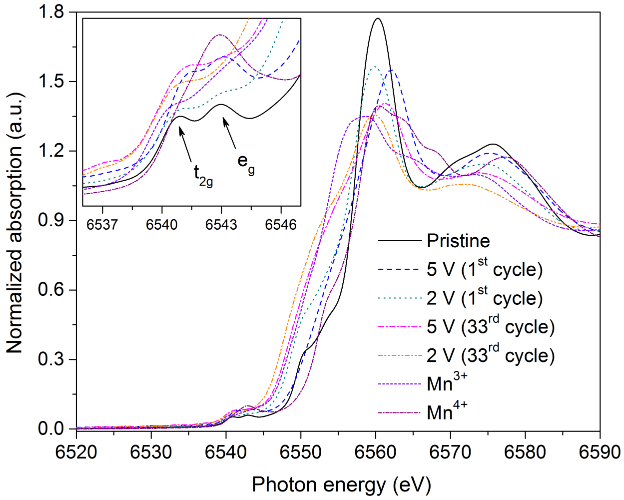

Figure 3: Normalized absorption spectra for various Li_2MnO_3 samples along with those of Mn^{3+} and Mn^{4+} reference compounds. The inset shows an enlarged pre-edge region.

As shown in Figure 3, the absorption spectra for various Li_2MnO_3 samples appear more complex than those of manganese reference compounds due to the presence of several points of intersection along the main edge where some of the spectra cross. Closer examination of these spectra reveals that the trend in chemical shifts varies widely before and after these intersection points. As shown in the inset, the pre-edge region in the pristine state is characterized by a splitting of Mn *3d* orbitals into t_{2g} and e_g orbitals. As the cathode is charged to 5 V, the intensity of the pre-edge peak increases and the peak splitting becomes less clear. When the cathode is discharged to 2 V, the intensity of the pre-edge peak decreases. For the cycled samples, changes in the pre-edge region are less obvious.

EXAFS

The comparison between the $\chi(k)$ signals of various Li_2MnO_3 samples in Figure 4a reveals that the EXAFS oscillations are reduced as soon as the cathode is charged to 5 V. In the corresponding Fourier transforms in Figure 4b, this is reflected by a preferential reduction in the amplitude of the 1^{st} shell of O atoms besides an overall damping of other shells. Qualitatively, $\chi(k)$ of the cycled-charged sample (i.e. the sample charged to 5 V during the 33^{rd} cycle) appears similar to that of the sample charged during the 1^{st} cycle, except that the signal is further damped. Besides clear reduction in the peak amplitudes, the higher order shells of Mn atoms (at ∼4.7 Å) and O atoms (at ∼5.3 Å) largely disappear upon cycling.

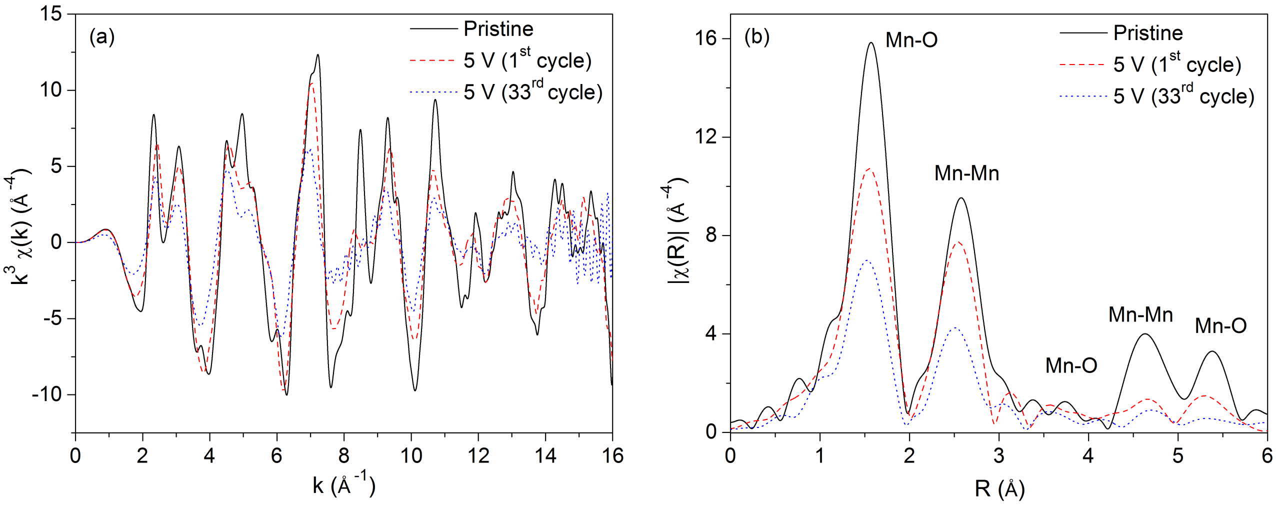

Figure 4: (a) k^3-weighted $\chi(k)$ signals and (b) their Fourier transforms for Li_2MnO_3 samples in the pristine state (solid black line), when charged to 5 V during the 1^{st} cycle (dashed red line) and when charged to 5 V during the 33^{rd} cycle (dotted blue line).

As shown in Figure 5a, every feature of the $\chi(k)$ signal corresponding to the pristine sample is reproduced when the cathode is discharged to 2 V during the 1^{st} cycle, however, with reduced amplitudes. This is also indicated by close similarities in their Fourier transforms in Figure 5b. Again, the EXAFS signals corresponding to the cycled-discharged sample (i.e. the sample discharged to 2 V during the 33^{rd} cycle) appear similar to those of the sample discharged during the 1^{st} cycle, however, the higher order shells are damped.

EXAFS data in the pristine state were fitted by the monoclinic structure of Li_2MnO_3 ($C2/m$)[32] (Figure 6). Best-fit parameters are reported in Table S2 in SI. A product of S_0^2 and the number of coordinating atoms (N) in a given shell determines its amplitude. As a result, these two parameters for a given shell cannot be varied independently in a fit. This

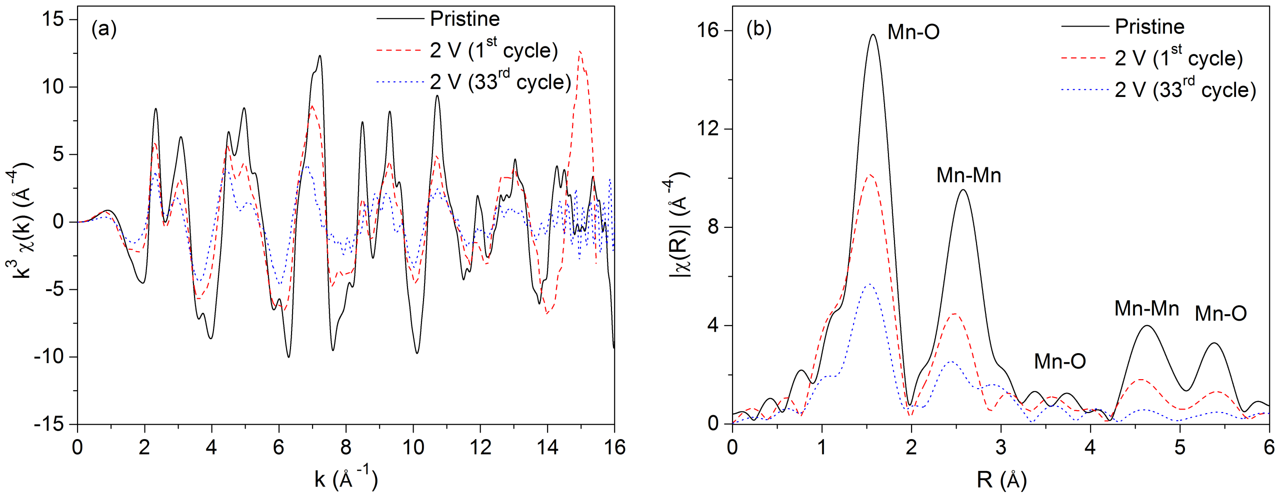

Figure 5: (a) k^3-weighted $\chi(k)$ signals and (b) their Fourier transforms for Li$_2$MnO$_3$ samples in the pristine state (solid black line), when discharged to 2 V during the 1st cycle (dashed red line) and when discharged to 2 V during the 33rd cycle (dotted blue line).

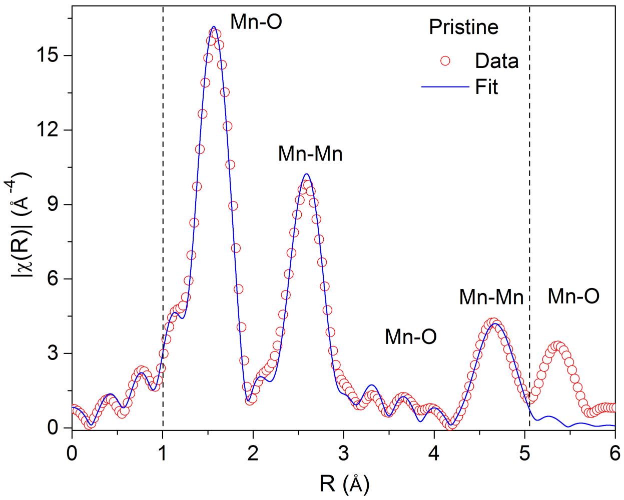

Figure 6: EXAFS fit to the data of Li$_2$MnO$_3$ sample in the pristine state. The dotted lines indicate the fitting range.

can be realized by the fact that when the number of oxygen nearest neighbors (O_{N-N}) in the pristine Li$_2$MnO$_3$ was constrained to that obtained from the theoretical model, the fit refined S$_0^2$ to 0.76(4) which is consistent with S$_0^2$ values obtained by fitting the EXAFS data of other manganese reference compounds. Conversely, when S$_0^2$ was constrained to 0.76, the fit refined O_{N-N} to 6.0(4) which is consistent with the fact that in Li$_2$MnO$_3$ Mn^{4+} is octahedrally coordinated by oxygen. Additionally, σ^2 which represents disorder in the material also affects the amplitude and, therefore, the terms $S_0^2 \times N$ and σ^2 for a given coordination shell are highly correlated. Thus, determining N in highly disordered systems remains a challenge. The most significant contribution to EXAFS signal is due to backscattering of ejected photoelectrons from the nearest neighbors (i.e. O_{N-N} in case of Li_2MnO_3). The contribution from outer coordination shells decreases due to increased inelastic losses as photoelectrons propagate in the material. Since S_0^2 is the property of absorbing atoms, it is transferable between compounds where the absorbing atom in question is coordinated by the same type of nearest neighbors. On the other hand, σ^2 cannot be estimated a priori. Thus, in situations where structural changes are to be followed as a result of any physical or chemical change that the sample has undergone, S_0^2 can be estimated from the starting material. From this aspect, S_0^2 determined from the pristine sample of Li_2MnO_3 was regarded as best estimate since it has known oxygen coordination. S_0^2 thus determined was constrained when structural changes due to changes in O_{N-N} in the material were to be estimated.

It has been reported that Li extraction from Li_2MnO_3 occurs with a simultaneous loss of oxygen, giving rise to the formation of a layered MnO_2-type structure (trigonal, $R\bar{3}m$) with the average valence state of Mn remaining unchanged at 4+.[11] There are also reports claiming the formation of either layered MnO_2-type structure or α-MnO_2-type structure (tetragonal, $I4/m$) upon chemical delithiation of Li_2MnO_3.[33,34] In order to assess such reports, the EXAFS data of the sample charged to 5 V during the 1^{st} cycle were fitted using the crystal structures of α-MnO_2 and layered MnO_2. The best fit was obtained assuming the layered MnO_2 structure (Figure 7a). Best-fit parameters are reported in Table S3 in SI. The fit constraining S_0^2 to 0.76 refined O_{N-N} to 5.6(8) which is high considering that oxygen is released from the material.

It has been proposed that Li re-insertion into layered MnO_2 occurs with a simultaneous reduction of Mn^{4+} to Mn^{3+}, thus forming $LiMnO_2$.[6,35] Therefore, an attempt was made to fit the EXAFS data of the sample discharged to 2 V during the 1^{st} cycle by a layered $LiMnO_2$ structure ($R\bar{3}m$). However, there was no agreement between the data and theory. The data

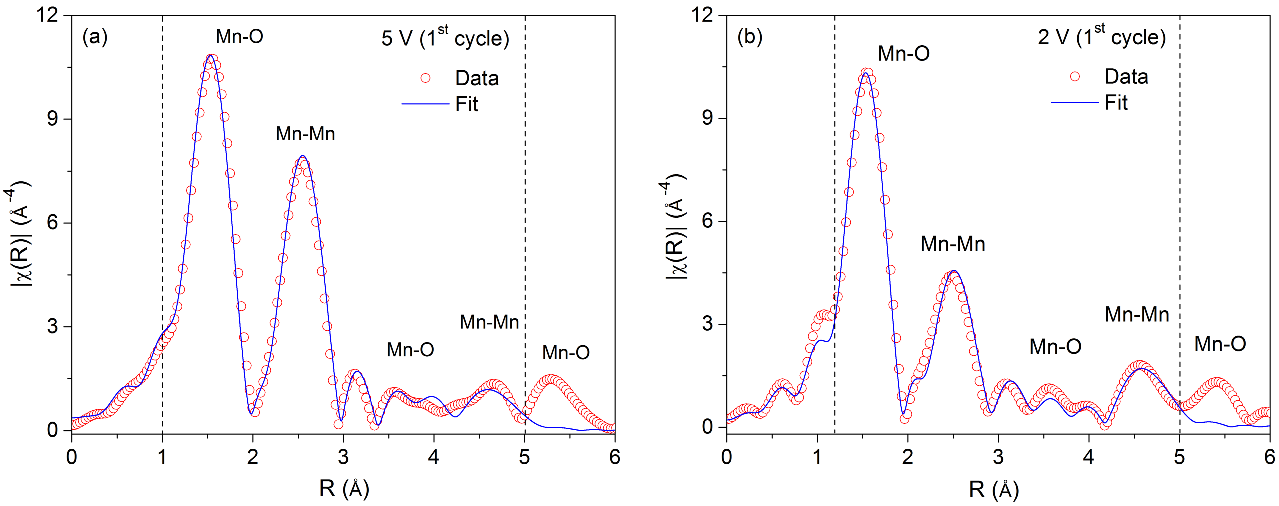

Figure 7: EXAFS fits to the data of Li_2MnO_3 samples (a) When charged to 5 V and (b) When discharged to 2 V during the 1^{st} cycle.

were rather explained by a Li_2MnO_3 structure (Figure 7b). Best-fit parameters are reported in Table S4 in SI. The fit refined O_{N-N} to 4.3(4) when S_0^2 was constrained to 0.76.

It has been claimed that prolonged cycling of Li_2MnO_3 gives rise to the formation of $LiMn_2O_4$-type spinel phase.[14] Therefore, an attempt was made to refine the fraction of such spinel phase in the cycled samples. However, there was no good agreement between the data and theory. For comparison, the EXAFS data of $LiMn_2O_4$ spinel is shown in Figure 8.

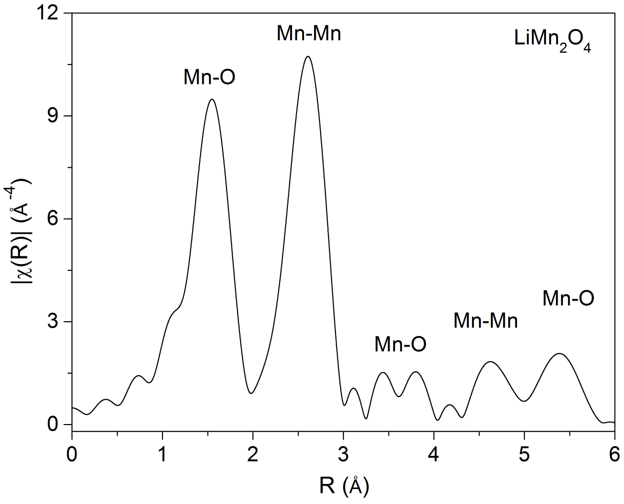

Figure 8: EXAFS data of $LiMn_2O_4$ spinel.

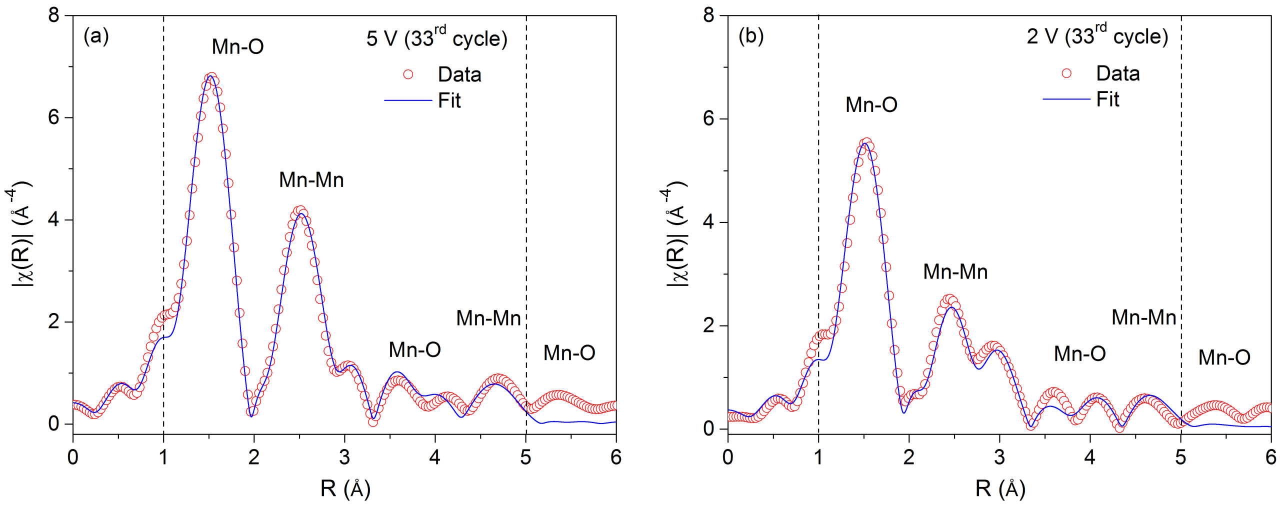

Figure 9: EXAFS fits to the data of Li_2MnO_3 samples (a) When charged to 5 V and (b) When discharged to 2 V during the 33^{rd} cycle.

Qualitatively, the EXAFS data of the cycled samples appear similar to those of their counterparts during the 1^{st} cycle. As a result, a layered MnO_2 structure was assumed to fit the data of the cycled-charged sample. When S_0^2 was constrained to 0.76, the fit refined O_{N-N} to 3.3(4) which is very low considering the weak pre-edge peak of the cycled samples (inset in Figure 3), suggesting octahedral coordination. This fit result emphasizes the effect of an observed reduction in the EXAFS signals upon cycling. A gradually declining electrochemical performance of the cell during cycling (Figure 1b) suggests a gradual loss in the intercalation ability of the material. Therefore, a parameter describing an effective concentration of electrochemically active material, X_{eff}, was introduced to the model such that the amplitude of each coordination shell of the cycled samples was represented by the term $S_0^2 \times N \times X_{eff}$. A fit constraining S_0^2 to 0.76 and O_{N-N} to 4.3, refined X_{eff} to 0.73(6) (Table S5 in SI) with a good agreement with the data as shown in Figure 9a. Similarly, the EXAFS data of the cycled-discharged sample were explained by a Li_2MnO_3 structure (Figure 9b). A fit constraining S_0^2 to 0.76 and O_{N-N} to 4.3, refined X_{eff} to 0.61(5) (Table S6 in SI).

A comparison between the metal-ligand bond length of various Li_2MnO_3 samples is shown in Figure 10. The average Mn-O bond length in the pristine state is slightly higher than

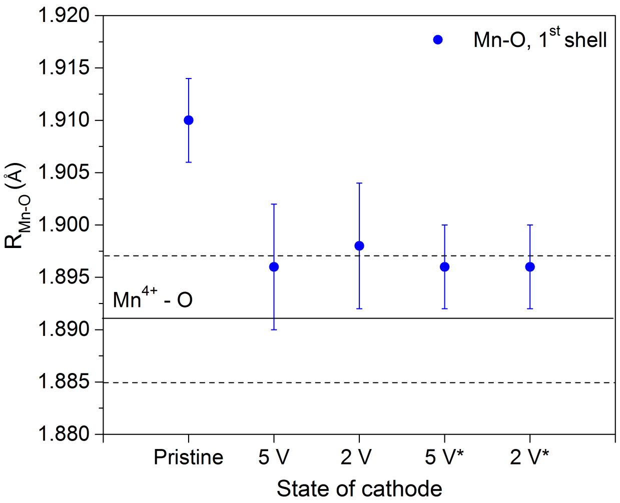

Figure 10: Comparison of the metal-ligand bond length for the electrochemically cycled Li_2MnO_3 samples during the 1^{st} and 33^{rd} cycles. The asterisk (*) represents the charged-discharged samples during the 33^{rd} cycle. The solid line indicates the average Mn^{4+}-O bond length obtained by fitting the EXAFS data of MnO_2 reference compound and dotted lines indicate statistical uncertainties of the fitted value.

that of Mn^{4+}-O. As the cathode is charged to 5 V, this bond length shortens and becomes similar to that of Mn^{4+}-O. The bond length, however, remains unchanged during subsequent cycling.

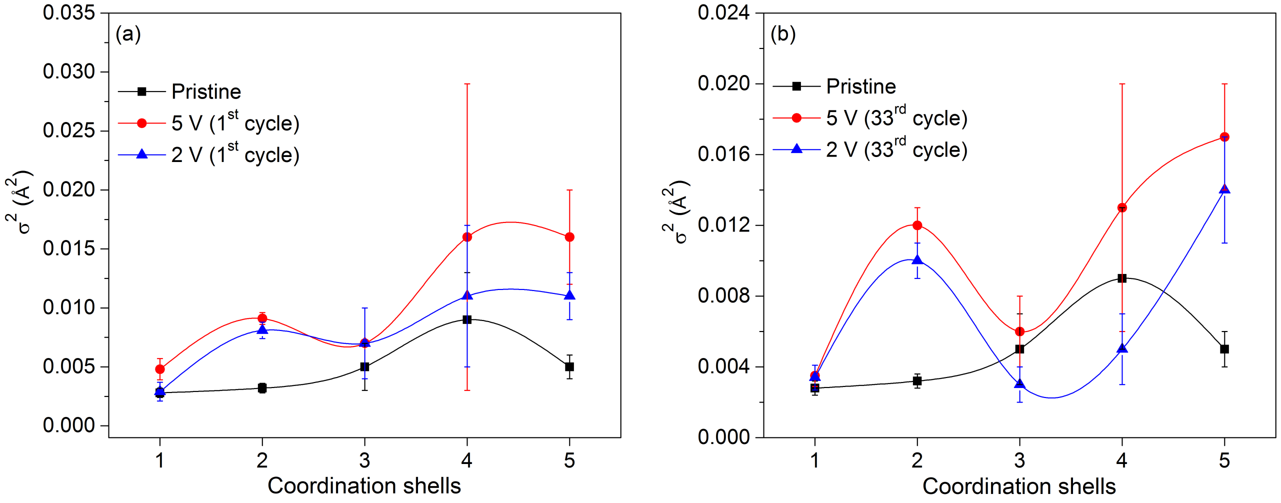

Figure 11: Structural disorder in charged-discharged samples of Li_2MnO_3 (a) During the 1^{st} cycle and (b) During the 33^{rd} cycle.

σ^2 is the distribution of the backscattering atoms around their mean position measured with respect to the central absorbing atom. This distribution can be either caused by thermal vibrations (thermal disorder) or by static displacement of atoms (structural disorder).[36,37] Since all samples in the present study are characterized at the same temperature (i.e. room temperature), a systematic variation in their σ^2 can be attributed to structural disorder introduced in the material as a result of electrochemical cycling, while neglecting thermal disorder. As shown in Figure 11a, the pristine sample exhibits the smallest, while the charged sample exhibits the largest disorder for all shells during the 1^{st} cycle. The structural disorder for the discharged sample is intermediate and in fact, appears to revert back to that of the pristine state. Note that σ^2 associated with the 4^{th} shell is particularly large and ill-refined for the charged sample, while it is small and better refined for the discharged sample. The structural disorder associated with the cycled samples is shown in Figure 11b. The cycled-charged sample has larger disorder than the cycled-discharged sample for all shells. However, the trend is less clear beyond the 2^{nd} shell.

The statistical EXAFS fit parameters for various Li_2MnO_3 samples are reported in Table S7 in SI. A good agreement between the data and theory for all samples can be seen by their R-factors that are < 0.02.

Discussion

XANES

1s→3d transitions are forbidden by dipole rules in centrosymmetric configurations such as in regular octahedral symmetry. However, with increasing distortion from ideal octahedral symmetry, the probability of a transition to *d*-orbitals increases. For tetrahedral symmetry, the metal-ligand orbital intermixing results in dipole-allowed *1s→3d* transitions with an intense pre-edge peak.[31,38] As shown in Figure 2a, MnO with perfect octahedral symmetry has the lowest pre-edge peak intensity. As the distortion in octahedral symmetry increases in the order Mn_2O_3[39] → $LiMn_2O_4$[40] → MnO_2,[41] the intensity of the pre-edge peak increases correspondingly. $KMnO_4$ with tetrahedral symmetry[42] has the highest pre-edge peak intensity. Moreover, MnO with Mn^{2+} exhibits the longest Mn-O bond length, while $KMnO_4$ with Mn^{7+} has the shortest Mn-O bond length among all manganese reference compounds. Thus, the strength of the pre-edge peak can be correlated to the local coordination symmetry around the absorbing atom and the average metal-ligand bond length.

The metal-ligand bond length determines the extent to which orbital intermixing takes place. As a result of this intermixing, the repulsive forces between the electrons increase the energies of these orbitals. Thus, metal *d*-orbitals split into t_{2g} and e_g orbitals.[31,38] This can be realized by observing the pre-edge peaks of various manganese reference compounds (inset in Figure 2a). MnO is a model octahedral compound, thus showing a very faint pre-edge peak. A higher valence state of Mn in Mn_2O_3 implies a shorter average Mn-O bond length than in MnO, which leads to higher electronic repulsions and higher orbital energies. As a result, the onset of pre-edge peak splitting in the Mn_2O_3 spectrum is clearly visible. This peak splitting becomes more pronounced with a further increase in the average valence state of Mn to $Mn^{3.5+}$ or shortening of the average Mn-O bond length in $LiMn_2O_4$. For Li_2MnO_3, where Mn^{4+} is octahedrally coordinated by O^{2-}, the peak splitting is maximum and best resolved (inset in Figure 3), as has been reported previously.[18,43] A similar peak splitting phenomenon is also observed at the Fe K-edge of $LiFePO_4$,[31,38] and is often known as crystal field splitting.

Empirically, a chemical shift in the absorption spectra can be correlated to the formal valence state of an absorbing atom.[30,44] However, besides the valence of an absorbing atom, chemical shifts are also affected by other structural features such as type, symmetry and number of nearest neighbors, character of bond etc.[30] Also, the extent to which each of these features contribute to the chemical shift varies widely from material to material. The observed unambiguous chemical shift for various manganese reference compounds in Figure 2a is the simplest example. However, for the samples of interest determining the chemical shift can be quite complex. For instance, it is difficult to judge the chemical shift among various Li_2MnO_3 samples in Figure 3 since there are several points along the main edge where spectra cross. In this situation, an estimation of the valence state depends on the reference point chosen. Thus, the approach involving the determination of the valence state of an absorbing atom from the observed chemical shift is strictly empirical, highly subjective[18,29] and sometimes confusing.[43] Contrary to this, the average metal-ligand bond length obtained by fitting the EXAFS data provides more reliable information about the valence state of an absorbing atom since this bond length primarily depends on the ionic radius of the absorbing atom and, in turn, on its valence state as demonstrated in Figure 2b.

EXAFS

Structural changes during the 1^{st} charge

XAS can distinguish between different atom types based on their ability to scatter the ejected photoelectron, which in turn depends on their atomic number Z. Despite Mn ($Z = 25$) having a higher atomic number than O ($Z = 8$), the amplitude of the signal coming from the 1^{st} shell of O atoms is higher than from the 2^{nd} shell of Mn atoms in Li_2MnO_3 (Figure 6). This can be attributed to a higher overall concentration of $\frac{O}{Mn}$ atoms (i.e. $O : Mn = 3 : 1$) and an ordered structure of Li_2MnO_3 resulting in six O atoms in the 1^{st} shell, but only three Mn atoms in the 2^{nd} shell (see Table S2 in SI). Thus, the ratio of the amplitudes of the first two Fourier transform peaks, i.e. the $\frac{Mn-O}{Mn-Mn}$ ratio, being >1 is the EXAFS signature reflecting the atomic arrangements of the Li_2MnO_3 structure.

A preferential reduction in the amplitude of the 1^{st} shell of O atoms besides an overall damping of other shells at 5 V (Figure 4b) is consistent with previous reports,[18] and can be attributed, respectively, to the oxygen loss and structural disorder introduced thereby upon Li extraction. This can be explained by the fact that the best fit to the EXAFS data at 5 V (Figure 7a) is based on a layered MnO_2 structure, which has not only a reduced concentration of $\frac{O}{Mn}$ atoms but is also a disordered form of Li_2MnO_3.[14] Also, an increase in the σ^2 parameter for each coordination shell of the charged sample (Figure 11a) confirms the disorder introduced into the material by Li extraction. Consistent observation has been reported in the form of a loss of superlattice reflections in the XRD pattern of Li_2MnO_3 upon Li extraction.[18] Thus, Li extraction occurs with a concurrent removal of oxygen through its oxidation according to[45] :

$$\underbrace{\mathrm{Li_2MnO_3}}_{C2/m\,(\mathrm{O3-type})} \xrightarrow{\mathrm{Charge}} \underbrace{\mathrm{Li_{2(1-y)}\,MnO_{3-y}}}_{R\bar{3}m\,(\mathrm{O3-type})} + \underbrace{\mathrm{2y\,Li^{+}\,+y\,O^{2-}}}_{\text{``y Li}_2\text{O''}} + \mathrm{2y\,e^{-}} \qquad (0 \geq \mathrm{y} \geq 1). \quad (1)$$

However, fitting the EXAFS data of the charged sample refined O_{N-N} to 5.6(8) (Table S3 in SI) which is high considering the fact that oxygen is released from the material during activation. Nevertheless, changes in the characteristic EXAFS signals of the material during charge clearly suggest atomic rearrangements as a result of oxygen loss. The static disorder introduced into the material increases σ^2 corresponding to the 1^{st} shell of oxygen atoms (Figure 11a) and as a result of its high correlation with O_{N-N} (of the order of 0.88), the fit overestimated the value of O_{N-N} despite oxygen deficiency in the material. The observed shortening of the average Mn-O bond length upon charge (Figure 10) can be attributed to these atomic rearrangements in the material due to oxygen release. Consistent observations have been reported in the form of a lattice contraction upon Li extraction from Li_2MnO_3.[18,35]

Despite this structural modification, the $\frac{Mn-O}{Mn-Mn}$ ratio remains >1 for the charged sample (Figure 7a), which suggests that the material retains its original Li_2MnO_3-like character even upon Li extraction. Thus, Li extraction does not completely destroy the ordering of Li and Mn within the $[Li_{1/3}Mn_{2/3}]O_2$ slabs,[35] and that not all the extracted charge corresponds to oxygen release only. Partial oxidation of oxygen anions can also supply electrons to the external circuit without releasing oxygen from the material.[43,46–48] Similarly, electrolyte oxidation[49–51] can also contribute to the observed charge capacity during activation. It is possible that H^+ generated as a result of electrolyte oxidation could displace electrochemically extracted Li^+ in the structure.[13–15,35,45] A similar Li^+-H^+ exchange mechanism has been observed for lithium manganese oxide spinels.[52,53]

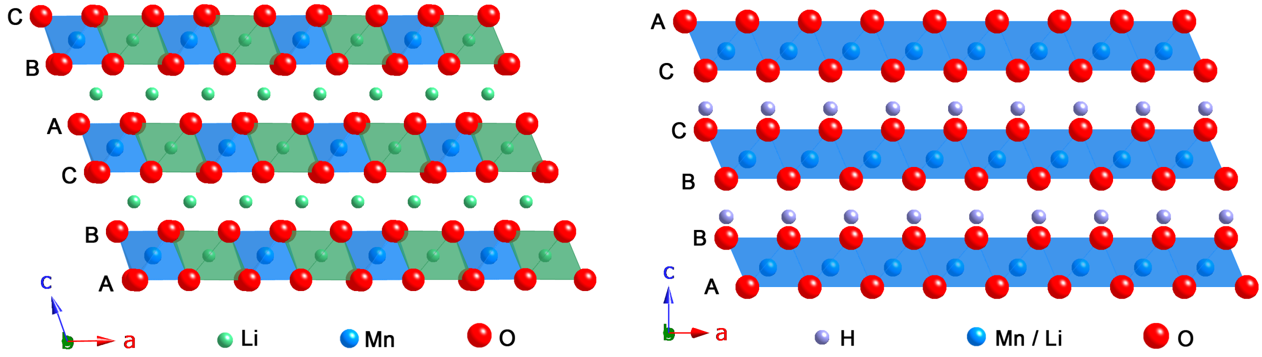

(a) O3 structure (ABCABC stacking)

(b) P3 structure (ABBCCA stacking)

Figure 12: Stacking sequence of close-packed oxygen layers in (a) O3 structure of Li_2MnO_3 ($C2/m$)[32] and (b) P3 structure ($R\bar{3}m$) of proton-exchanged material.[54] Note that O-H-O bonds are asymmetric in P3 structure.

The Li^+-H^+ exchange mechanism is also supported in Li_2MnO_3 by the observed change in the stacking sequence of oxygen layers from O3-type (ABCABC) to P3-type (ABBCCA) due to the presence of protons in the interslab region and strong O-H-O bonding.[14,35] For comparison, O3-type and P3-type structures are shown in Figure 12. The ordered atomic arrangements of O3 structure in the pristine state produced well-defined Fourier transform peaks between 3 - 4.2 Å in Figure 6. These peaks correspond to O atoms located at the boundaries of the neighboring $[\mathrm{Li}_{1/3}\mathrm{Mn}_{2/3}]\mathrm{O}_2$ slabs and are separated by interslab Li atoms (Figure 12a). For the charged sample, these peaks are replaced by a broad diffuse structure (Figure 7a). Correspondingly, σ^2 associated with the 4^{th} shell, which represents O atoms of the neighboring slabs increases abruptly and remains ill-refined upon charge (Figure 11a). Both, smeared EXAFS peaks and large ill-refined σ^2 suggest a large static displacement in the position of O atoms of the neighboring slabs and, in turn, can be correlated to a change in the stacking sequence of oxygen layers. Thus, the presence of H^+ in the interslab region, as a result of Li^+-H^+ exchange, shears the oxygen layers due to strong O-H-O bonding and alters their stacking sequence from O3-type to P3-type according to :

$$\underbrace{\mathrm{Li}^{+}_{\mathrm{x}+\delta}\mathrm{Mn}^{4+}\mathrm{O}^{2-}_{3-\mathrm{y}}}_{R\bar{3}m\,(\mathrm{O3-type})} \xrightarrow{\mathrm{Li}^{+}-\mathrm{H}^{+}\ \text{exchange and charge}} \underbrace{\mathrm{H}^{+}_{\mathrm{x}}\mathrm{Mn}^{4+}\mathrm{O}^{-2+\delta}_{3-\mathrm{y}}}_{R\bar{3}m\,(\mathrm{P3-type})} + (\mathrm{x}+\delta)\,\mathrm{Li}^{+} + (\mathrm{x}+\delta)\,\mathrm{e}^{-}. \tag{2}$$

Structural changes during the 1^{st} discharge

Several reports have claimed that Li re-insertion into layered MnO_2 gives rise to the formation of LiMnO_2 with the concurrent reduction of Mn^{4+} to Mn^{3+}.[6,35] According to these reports, the local structure of the discharged sample should be identical to that of the charged sample and the proposed reduction of Mn^{4+} to Mn^{3+} should be accompanied by an increase in the average Mn-O bond length. Contrary to these, the EXAFS data of the discharged sample (Figure 7b) appear identical to those of the pristine sample (Figure 6), however, with reduced amplitudes and the average Mn-O bond length remains unchanged from that of the charged sample (Figure 10). Both these results contradict the proposed hypothesis about Li re-insertion into layered MnO_2. A specific discharge capacity of 200 mAh/g during the 1^{st} cycle (Figure 1a) suggests that a significant amount of Li is re-inserted into the material. This could have happened by exchanging already present H^+ in the structure with Li^+.[14] Discharge could then involve the reduction of partially oxidized oxygen anions of active material,[43,46–48] and possibly that of electrolyte species which could consume H^+ driven out of the material.[14]

Qualitative similarities between the EXAFS data of the pristine and discharged samples suggest structural re-ordering upon Li re-insertion. This is consistent with a reduction in the σ^2 parameter for the coordination shells of the discharged sample (Figure 11a). However, since permanent disorder caused by oxygen removal cannot be reverted, the discharged sample exhibits slightly higher disorder than the pristine sample. Due to this and despite qualitative similarities, the EXAFS amplitudes for the discharged sample are slightly reduced than those of the pristine sample. The value of O_{N-N} refined to 4.3(4) for the discharged sample (Table S4 in SI) should not be interpreted as tetrahedral coordination around Mn atoms, since the pre-edge region for the discharged sample is characterized by a weak pre-edge peak quite similar to that of the pristine sample (inset in Figure 3) rather suggesting octahedral coordination. These evidences suggest that the material regains its ordered Li_2MnO_3-type character upon Li re-insertion. As a result, σ^2 corresponding the 1^{st} shell of O atoms decreases and becomes similar to that of the pristine state (Figure 11a). Due to this, the fit could correctly estimate oxygen deficiency in the material by refining O_{N-N} to 4.3(4) for the discharged sample.

The Fourier transform peaks between 3 - 4.2 Å representing O atoms of the neighboring slabs reappear upon discharge (Figure 7b). Correspondingly, σ^2 associated with these O atoms (4^{th} shell) decreases (Figure 11a). Both these results suggest a change in the stacking sequence of oxygen layers from P3-type back to the original O3-type and are in good agreement with an earlier report of Rossouw et al.[55] where the XRD pattern of a re-lithiated sample closely resembled that of the parent Li_2MnO_3. Thus, Li re-insertion reverts the stacking sequence of oxygen layers from P3-type back to the original O3-type according to :

$$\underbrace{\mathrm{H_x^+Mn^{4+}O_{3-y}^{-2+\delta}}}_{R\bar{3}m\,\mathrm{(P3-type)}} + \mathrm{(x+\delta)\,Li^+} + \mathrm{(x+\delta)\,e^-} \xrightarrow{\mathrm{H^+-Li^+\ exchange\ and\ discharge}} \underbrace{\mathrm{Li_{x+\delta}^+Mn^{4+}O_{3-y}^{2-}}}_{C2/m\,\mathrm{(O3-type)}} + \mathrm{x\,H^+}. \tag{3}$$

The resultant structure upon discharge is similar to that of the parent Li_2MnO_3, except that it contains less Li and O. The driving force for such structural reversion is believed to be the relaxation of strained oxygen layers by displacing H^+ in the interslab region by Li^+.

Structural changes upon cycling

It has been claimed that prolonged cycling of Li_2MnO_3 gives rise to the formation of $LiMn_2O_4$-type spinel phase.[14] This claim is supported by qualitative similarities between the electrochemical profiles of cycled Li_2MnO_3 and $LiMn_2O_4$[14] and the fact that the formation of $LiMn_2O_4$ spinel phase from layered $LiMnO_2$ that presumably forms during the 1^{st} discharge is favored.[56,57] However, the EXAFS data of the discharged sample during the 1^{st} cycle (Figure 7b) clearly suggest that Li re-insertion into layered MnO_2 gives rise to the formation of Li_2MnO_3-type structure. This result is in conflict with the existing hypothesis and raises doubts about the formation of a spinel-like phase upon cycling. Previously, Paik et al.[35] have also expressed ambiguity about the formation of a spinel-like phase upon cycling. Quite contrarily, a TEM investigation by Gu et al.[58] revealed the presence of randomly oriented, extremely small domains of $LiMn_2O_4$-type spinel phase embedded within the amorphous surrounding resulting from the breakdown of the parent lattice of Li_2MnO_3 upon cycling. Thus, there exist contradicting views about structural modifications in Li_2MnO_3 upon cycling.

The crystallographic difference between layered Li_2MnO_3 and spinel $LiMn_2O_4$ gives rise to distinct EXAFS signals (Figures 6 and 8). A major difference lies in their $\frac{Mn-O}{Mn-Mn}$ ratios. Based on this criterion, the local structure of the cycled samples (Figure 9) is more similar to their counterparts during the 1^{st} cycle (Figure 7) than to $LiMn_2O_4$. While the formation of the domains of $LiMn_2O_4$-type spinel phase upon cycling as observed during TEM investigation[58] cannot be ruled out, the presented EXAFS data of the cycled samples suggest otherwise. This discrepancy between the TEM and XAS investigations should be judged in the context of the investigated sample volume by both these techniques. Previously, Shao-Horn et al.[59] reported that an extremely small sampling size in TEM investigation may lead to systematically biased conclusions. In case of the formation of a spinel-like phase even on the particle surface,[58] a corresponding change in the EXAFS data of the material is expected since XAS in the transmission mode provides information from both surface and bulk of all particles within the illuminated sample volume of at least a few cubic millimeters. Contrary to this, the observed reduction in the EXAFS data of the cycled samples (Figures 4b and 5b), while maintaining the similar characteristic features as observed for the samples during the 1^{st} cycle suggests structural degradation of the material during cycling. This effect is analogous to the broadening of diffraction peaks in the XRD pattern of a material that loses crystallinity. In our opinion, random atomic arrangements caused by deteriorating structural changes that occur in the material during cycling may appear on an extremely local field of view of TEM as randomly oriented "spinel-like" domains. The best fit to the EXAFS data of the cycled-charged sample is by a layered MnO_2 structure and to those of the cycled-discharged sample is by a Li_2MnO_3 structure. These fit results suggest that the fraction of electrochemically active material is reduced to $\sim$60 - 70 % up to the 33^{rd} cycle which is consistent with the reported structural degradation of the material[58] and, in turn, explains the observed decline in its electrochemical performance during cycling. It is reasonable to constrain the value of O_{N-N} for the cycled samples to that obtained during the 1^{st} cycle for the obvious reason that oxygen is not released during each subsequent cycle, since under this situation the material would be completely depleted of oxygen anions after a few cycles. However, the weak pre-edge peak corresponding to the charged and discharged samples during the 33^{rd} cycle (inset in Figure 3) clearly suggests that local coordination symmetry around central Mn atoms is maintained as octahedral.

These results lead us to two major conclusions. First, the structural changes during the 33^{rd} cycle are similar to those observed during the 1^{st}, however, the fraction of electrochemically active material is gradually reduced up to the 33^{rd} cycle. Second, oxygen removal occurs only during activation of the material in the 1^{st} cycle. As observed during the 1^{st} cycle, structural disorder for the cycled-charged sample is higher than for the cycled-discharged sample (Figure 11b). However, the trend is less clear beyond the 2^{nd} shell. It should be noted that structural "visibility" for the cycled samples is also limited to the first two shells as indicated by well-defined Fourier transform peaks. Higher order shells of Mn atoms (at ~ 4.7 Å) and O atoms (at ~ 5.4 Å) clearly visible during the 1^{st} cycle are reduced during the 33^{rd} cycle (Figures 4b and 5b). These shells represent Mn and O atoms from the neighboring $[\mathrm{Li}_{1/3}\mathrm{Mn}_{2/3}]\mathrm{O}_2$ slabs. These results suggest that atomic arrangements within an individual $[\mathrm{Li}_{1/3}\mathrm{Mn}_{2/3}]\mathrm{O}_2$ slab are intact. However, the stacking sequence of subsequent slabs is disturbed upon cycling.

The average Mn-O bond length for the cycled samples (Figure 10) remains unchanged from that of Mn^{4+}-O, which rules out the conventional charge compensation mechanism involving the $\mathrm{Mn}^{3+}/\mathrm{Mn}^{4+}$ redox reaction. Therefore, the observed charge-discharge capacities during subsequent cycles must have different origins. Possibly, oxygen anions of active material participate in unusual redox processes[43,46–48] and repetitive, irreversible oxidation of electrolyte species occurs, since both these processes could supply electrons to the external circuit and contribute to the observed charge capacity. Protons generated as a result of electrolyte oxidation could displace electrochemically extracted Li in the interslab region and alter the stacking sequence of oxygen layers from O3-type to P3-type according to :

$$\underbrace{\mathrm{Li}^{+}_{\mathrm{x}+\delta}\mathrm{Mn}^{4+}\mathrm{O}^{2-}_{3-\mathrm{y}}}_{C2/m\,(\mathrm{O3-type})} \xrightleftharpoons[\mathrm{H^{+}-Li^{+}\ exchange\ and\ discharge}]{\mathrm{Li^{+}-H^{+}\ exchange\ and\ charge}} \underbrace{\mathrm{H}^{+}_{\mathrm{x}}\mathrm{Mn}^{4+}\mathrm{O}^{-2+\delta}_{3-\mathrm{y}}}_{R\bar{3}m\,(\mathrm{P3-type})} + (\mathrm{x}+\delta)\,\mathrm{Li}^{+} + (\mathrm{x}+\delta)\,\mathrm{e}^{-}. \tag{4}$$

Subsequent discharge could involve the reduction of partially oxidized oxygen anions along with electrolyte species and Li re-insertion could occur by displacing already present protons in the material with a concurrent change in the oxygen stacking sequence from P3-type back to the original O3-type (Equation (4)). Such repetitive shearing of oxygen layers during each subsequent cycle could lead to the loss of crystallinity of the material and consequently to the loss of its intercalation ability during cycling. The observed cleavage in Li_2MnO_3 particles along the (001) plane[45] can be explained in terms of shearing of individual $[Li_{1/3}Mn_{2/3}]O_2$ slab due to changing stacking sequence of oxygen layers. Moreover, the cycling curve of Li_2MnO_3 in Figure 1b does not show any plateau where fading levels off and at which the electrochemical performance of Li_2MnO_3 corresponds to that of $LiMn_2O_4$ spinel. In fact, fading starts right from the 1^{st} cycle and continues even beyond the 33^{rd} cycle. This suggests a continuous loss in the intercalation ability of the material as a result of continuous structural degradation during cycling. Since the suggested Li^+-H^+ exchange mechanism could involve the repetitive consumption of electrolyte species, it would inevitably deteriorate the cell performance on the long term. However, the presented results clearly suggest that the capacity degradation is more likely to be caused by the structural degradation of active material rather than the dry-out of electrolyte.

Conclusions

Both XANES and EXAFS provide complementary information that helps to understand structural changes in Li_2MnO_3. The total charge capacity during activation can be attributed to the oxidation of oxygen anions and that of electrolyte. The concurrent removal of oxygen along with Li gives rise to the formation of a layered MnO_2-type structure, while maintaining a certain degree of Li and Mn ordering within its $[Li_{1/3}Mn_{2/3}]O_2$ slabs. Protons generated as a result of electrolyte oxidation displace electrochemically extracted Li^+ in the structure. The presence of protons in the interslab region shears the oxygen layers due to strong O-H-O bonding and alters their stacking sequence from O3-type (ABCABC) to P3-type (ABBCCA). Li re-insertion into layered MnO_2-type structure occurs by exchanging already present protons in the interslab region. The relaxation of strained oxygen layers caused by exchanging H^+ with Li^+ reverts their stacking sequence from P3-type back to the original O3-type. The resultant structure upon discharge closely resembles the parent Li_2MnO_3, however, it contains less Li and O. Mn^{4+} does not participate in electrochemical processes and its average valence state remains unchanged at 4+ at all times. Irreversible oxygen release occurs only during activation of the material in the 1^{st} cycle. During subsequent cycles, electrochemical processes could possibly involve unusual redox processes of oxygen anions of active material together with the repetitive, irreversible oxidation of electrolyte species :

$$\underbrace{\mathrm{Li}^{+}_{\mathrm{x}+\delta}\mathrm{Mn}^{4+}\mathrm{O}^{2-}_{3-\mathrm{y}}}_{C2/m\,(\mathrm{O3-type})} \xrightleftharpoons[\mathrm{H^{+}-Li^{+}\ exchange\ and\ discharge}]{\mathrm{Li^{+}-H^{+}\ exchange\ and\ charge}} \underbrace{\mathrm{H}^{+}_{\mathrm{x}}\mathrm{Mn}^{4+}\mathrm{O}^{-2+\delta}_{3-\mathrm{y}}}_{R\bar{3}m\,(\mathrm{P3-type})} + (\mathrm{x}+\delta)\,\mathrm{Li}^{+} + (\mathrm{x}+\delta)\,\mathrm{e}^{-}. \tag{5}$$

The proposed Li^+-H^+ exchange during each subsequent charge and discharge could involve a structural flip-over between O3-type ($C2/m$) and P3-type ($R\bar{3}m$) by repeated shearing of oxygen layers. This could deteriorate crystallinity of the material and consequently its electrochemical performance during cycling.

Acknowledgement

The authors acknowledge the financial support from the Europäischer Fonds für regionale Entwicklung (EFRE) under the project BATMAT (No. 200720132/35). RK acknowledges the financial support from the Hans-L. Merkle Stiftung of the Robert Bosch GmbH.

References

(1) Johnson, C.; Kim, J.-S.; Lefief, C.; Li, N.; Vaughey, J.; Thackeray, M. *Electrochem. commun.* **2004**, *6*, 1085–1091.

(2) Johnson, C.; Li, N.; Vaughey, J.; Hackney, S.; Thackeray, M. *Electrochem. commun.* **2005**, *7*, 528–536.

(3) Thackeray, M.; Kang, S.-H.; Johnson, C.; Vaughey, J.; Hackney, S. *Electrochem. commun.* **2006**, *8*, 1531–1538.

(4) Johnson, C. *J. Power Sources* **2007**, *165*, 559–565.

(5) Johnson, C.; Li, N.; Lefief, C.; Thackeray, M. *Electrochem. commun.* **2007**, *9*, 787–795.

(6) Thackeray, M.; Kang, S.-H.; Johnson, C.; Vaughey, J.; Benedek, R.; Hackney, S. *J. Mater. Chem.* **2007**, *17*, 3112–3125.

(7) Li, J.; Klöpsch, R.; Stan, M.; Nowak, S.; Kunze, M.; Winter, M.; Passerini, S. *J. Power Sources* **2011**, *196*, 4821–4825.

(8) Croy, J.; Balasubramanian, M.; Kim, D.; Kang, S.-H.; Thackeray, M. *Chem. Mater.* **2011**, *23*, 5415–5424.

(9) Croy, J.; Kim, D.; Balasubramanian, M.; Gallagher, K.; Kang, S.-H.; Thackeray, M. *J. Electrochem. Soc.* **2012**, *159*, A781–A790.

(10) Boulineau, A.; Croguennec, L.; Delmas, C.; Weill, F. *Solid State Ionics* **2010**, *180*, 1652–1659.

(11) Thackeray, M. *Prog. Solid State Chem.* **1997**, *25*, 1–71.

(12) Kalyani, P.; Chitra, S.; Mohan, T.; Gopukumar, S. *J. Power Sources* **1999**, *80*, 103–106.

(13) Robertson, A.; Bruce, P. *Chem. Commun.* **2002**, 2790–2791.

(14) Robertson, A.; Bruce, P. *Chem. Mater.* **2003**, *15*, 1984–1992.

(15) Armstrong, A.; Robertson, A.; Bruce, P. *J. Power Sources* **2005**, *146*, 275–280.

(16) Jain, G.; Yang, J.; Balasubramanian, M.; Xu, J. *Chem. Mater.* **2005**, *17*, 3850–3860.

(17) Pasero, D.; McLaren, V.; de Souza, S.; West, A. *Chem. Mater.* **2005**, *17*, 345–348.

(18) Yu, D.; Yanagida, K.; Kato, Y.; Nakamura, H. *J. Electrochem. Soc.* **2009**, *156*, A417–A424.

(19) Liu, W.; Farrington, G.; Chaput, F.; Dunn, B. *J. Electrochem. Soc.* **1996**, *143*, 879–884.

(20) Kelly, S.; Hesterberg, D.; Ravel, B. *Methods Soil Anal. Part 5*; 2008; Vol. 5; pp 387–463.

(21) Ravel, B.; Newville, M. *J. Synchrotron Radiat.* **2005**, *12*, 537–541.

(22) Ankudinov, A.; Ravel, B.; Rehr, J.; Conradson, S. *Phys. Rev. B* **1998**, *58*, 7565–7576.

(23) Rehr, J.; Stern, E.; Martin, R.; Davidson, E. *Phys. Rev. B* **1978**, *17*, 560–565.

(24) Stern, E.; Bunker, B.; Heald, S. *Phys. Rev. B* **1980**, *21*, 5521–5539.

(25) Teo, B. *EXAFS: Basic principles and data analysis*; Springer-Verlag Berlin, 1986; Vol. 10.

(26) Calvin, S. Relationship between electron delocalization and asymmetry of the pair distribution function as determined by x-ray absorption spectroscopy. Ph.D. thesis, 2001.

(27) Newville, M. Local thermodynamic measurements of dilute binary alloys using XAFS. Ph.D. thesis, 1995.

(28) Ravel, B. Ferroelectric phase transitions in oxide perovskites studied by XAFS. Ph.D. thesis, 1997.

(29) Yu, D.; Yanagida, K. *J. Electrochem. Soc.* **2011**, *158*, A1015–A1022.

(30) Wong, J.; Lytle, F.; Messmer, R.; Maylotte, D. *Phys. Rev. B* **1984**, *30*, 5596–5610.

(31) Haas, O.; Deb, A.; Cairns, E.; Wokaun, A. *J. Electrochem. Soc.* **2005**, *152*, A191–A196.

(32) Strobel, P.; Lambert-Andron, B. *J. Solid State Chem.* **1988**, *75*, 90–98.

(33) Rossouw, M.; Thackeray, M. *Mater. Res. Bull.* **1991**, *26*, 463–473.

(34) Rossouw, M.; Liles, D.; Thackeray, M.; David, W.; Hull, S. *Mater. Res. Bull.* **1992**, *27*, 221–230.

(35) Paik, Y.; Grey, C.; Johnson, C.; Kim, J.-S.; Thackeray, M. *Chem. Mater.* **2002**, *14*, 5109–5115.

(36) Sayers, D.; Stern, E.; Lytle, F. *Phys. Rev. Lett.* **1971**, *27*, 1204–1207.

(37) Rehr, J.; Albers, R. *Rev. Mod. Phys.* **2000**, *72*, 621–654.

(38) Deb, A.; Bergmann, U.; Cairns, E.; Cramer, S. *J. Synchrotron Radiat.* **2004**, *11*, 497–504.

(39) Geller, S.; Cape, J.; Grant, R.; Espinosa, G. *Phys. Lett. A* **1967**, *24A*, 369–371.

(40) Ouyang, C.; Shi, S.; Lei, M. *J. Alloys Compd.* **2009**, *474*, 370–374.

(41) Baur, W. *Acta Crystallogr.* **1976**, *B32*, 2200–2204.

(42) Marabello, D.; Bianchi, R.; Gervasio, G.; Cargnoni, F. *Acta Crystallogr., Sect. A: Found. Crystallogr.* **2004**, *A60*, 494–501.

(43) Ito, A.; Sato, Y.; Sanada, T.; Hatano, M.; Horie, H.; Ohsawa, Y. *J. Power Sources* **2011**, *196*, 6828–6834.

(44) Sapre, V.; Mande, C. *J. Phys. C: Solid State Phys.* **1972**, *5*, 793–797.

(45) Tang, W.; Kanoh, H.; Yang, X.; Ooi, K. *Chem. Mater.* **2000**, *12*, 3271–3279.

(46) Goodenough, J.; Kim, Y. *Chem. Mater.* **2010**, *22*, 587–603.

(47) Koga, H.; Croguennec, L.; Ménétrier, M.; Mannessiez, P.; Weill, F.; Delmas, C. *J. Power Sources* **2013**, *236*, 250–258.

(48) Koga, H.; Croguennec, L.; Ménétrier, M.; Douhil, K.; Belin, S.; Bourgeois, L.; Suard, E.; Weill, F.; Delmas, C. *J. Electrochem. Soc.* **2013**, *160*, A786–A792.

(49) Kanamura, K.; Toriyama, S.; Shiraishi, S.; Takehara, Z.-i. *J. Electrochem. Soc.* **1996**, *143*, 2548–2558.

(50) Kanamura, K. *J. Power Sources* **1999**, *81-82*, 123–129.

(51) Moshkovich, M.; Cojocaru, M.; Gottlieb, H.; Aurbach, D. *J. Electroanal. Chem.* **2001**, *497*, 84–96.

(52) Feng, Q.; Miyai, Y.; Kanoh, H.; Ooi, K. *Langmuir* **1992**, *8*, 1861–1867.

(53) Ammundsen, B.; Aitchison, P.; Burns, G.; Jones, D.; Rozière, J. *Solid State Ionics* **1997**, *97*, 269–276.

(54) Christensen, A.; Hansen, P.; Lehmann, M. *J. Solid State Chem.* **1977**, *21*, 325–329.

(55) Rossouw, M.; Liles, D.; Thackeray, M. *J. Solid State Chem.* **1993**, *104*, 464–466.

(56) Robertson, A.; Armstrong, A.; Bruce, P. *Chem. Mater.* **2001**, *13*, 2380–2386.

(57) Armstrong, A.; Paterson, A.; Robertson, A.; Bruce, P. *Chem. Mater.* **2002**, *14*, 710–719.

(58) Gu, M.; Belharouak, I.; Zheng, J.; Wu, H.; Xiao, J.; Genc, A.; Amine, K.; Thevuthasan, S.; Baer, D.; Zhang, J.-G.; Browning, N.; Liu, J.; Wang, C. *ACS Nano* **2012**, *7*, 760–767.

(59) Shao-Horn, Y.; Hackney, S.; Armstrong, A.; Bruce, P.; Gitzendanner, R.; Johnson, C.; Thackeray, M. *J. Electrochem. Soc.* **1999**, *146*, 2404–2412.

Supporting Information

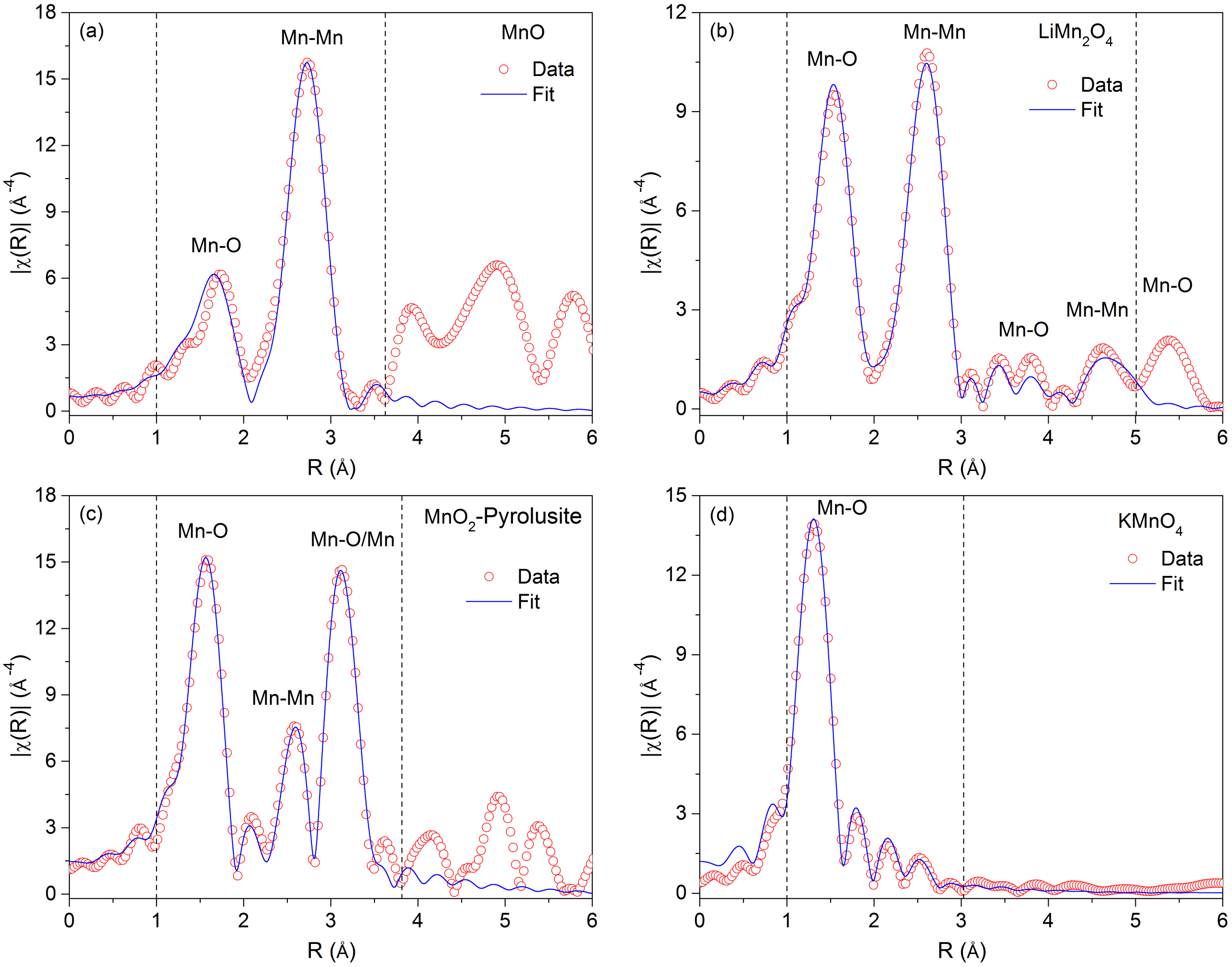

Figure S1: EXAFS fits to the data of various manganese reference compounds.

Table S1: EXAFS fit parameters for the 1^{st} shell of various manganese reference compounds.

Sample	R_{theory} (Å)	α_{fit}	ΔR (Å)	R_{fit} (Å)	R_{mean} (Å)	σ^2_{fit} (Å^2)
MnO	6×2.222	-0.032 (6)	-0.071 (12)	2.151 (12)	2.151 (12)	0.010 (2)
$LiMn_2O_4$	6×1.976	-0.035 (3)	-0.069 (6)	1.907 (6)	1.907 (6)	0.0049 (8)
MnO_2	2×1.878 4×1.891	0.002 (3)	0.004 (6) 0.004 (6)	1.882 (6) 1.895 (6)	1.891 (6)	0.0034 (7)
$KMnO_4$	2×1.612 1×1.613 1×1.613	0.014 (3)	0.023 (5) 0.023 (5) 0.023 (5)	1.635 (5) 1.636 (5) 1.636 (5)	1.636 (5)	0.0012 (4)

Table S2: EXAFS fit parameters for Li_2MnO_3 sample in the pristine state. The values in parentheses indicate uncertainties to the least significant digit(s). The parameters without uncertainties were constrained in the fit.

$S_0^2 = 0.76\,(4)$

$\Delta E_0 = 7.0\,(7)$

Path[a]	N_{degen}[b]	R_{theory}[c] (Å)	α_{fit}	ΔR[d] (Å)	R_{fit}[e] (Å)	σ^2_{fit} (Å^2)
Mn-O_{N-N}	2	1.904	-0.001 (2)	-0.002 (4)	1.902 (4)	0.0028 (4)
	2	1.912		-0.002 (4)	1.910 (4)	
	2	1.919		-0.002 (4)	1.917 (4)	
Mn-Mn	2	2.845	0.002 (1)	0.006 (3)	2.851 (3)	0.0032 (4)
	1	2.851		0.006 (3)	2.857 (3)	
Mn-O	2	3.513	0.001 (5)	0.004 (18)	3.517 (18)	0.005 (2)
	2	3.515		0.004 (18)	3.519 (18)	
	2	3.516		0.004 (18)	3.520 (18)	
	2	3.686		0.004 (18)	3.690 (18)	
Mn-O	2	4.388	0.005 (6)	0.022 (28)	4.410 (28)	0.009 (4)
	2	4.390		0.022 (28)	4.412 (28)	
	2	4.395		0.022 (28)	4.417 (28)	
	2	4.578		0.023 (28)	4.601 (28)	
	2	4.579		0.023 (28)	4.602 (28)	
	2	4.587		0.023 (28)	4.610 (28)	
	2	4.594		0.023 (28)	4.617 (28)	
	2	4.599		0.023 (28)	4.622 (28)	
	2	4.638		0.023 (28)	4.661 (28)	
	2	4.672		0.023 (28)	4.695 (28)	
	2	4.693		0.024 (28)	4.717 (28)	
	2	4.721		0.024 (28)	4.745 (28)	
Mn-Mn	4	4.929	0.006 (2)	0.030 (10)	4.959 (10)	0.005 (1)
	2	4.937		0.030 (10)	4.967 (10)	
	2	5.012		0.030 (10)	5.042 (10)	
	2	5.030		0.030 (10)	5.060 (10)	

[a] Scattering path from the theoretical model

[b] N_{degen} = Degeneracy of scattering paths from the theoretical model

[c] R_{theory} = Interatomic distances from the theoretical model

[d] $\Delta R = \alpha_{fit} \times R_{theory}$

[e] $R_{fit} = R_{theory} + \Delta R$

Table S3: EXAFS fit parameters for Li_2MnO_3 sample charged to 5 V during the 1st cycle.

$S_0^2 = 0.76$
$\Delta E_0 = 5.0\,(1.2)$

Path	N_{degen}	R_{theory} (Å)	α_{fit}	ΔR (Å)	R_{fit} (Å)	σ^2_{fit} (Å^2)
Mn-O_{N-N}	5.6 (8)	1.921	-0.013 (3)	-0.025 (6)	1.896 (6)	0.0048 (9)
Mn-Mn	6	2.816	0.019 (3)	0.054 (9)	2.870 (9)	0.0091 (5)
Mn-O	6 2	3.409 3.661	0.021 (6)	0.072 (22) 0.077 (22)	3.481 (22) 3.738 (22)	0.007 (3)
Mn-O	12 12	4.422 4.619	-0.007 (17)	-0.031 (79) -0.032 (79)	4.391 (79) 4.587 (79)	0.016 (13)
Mn-Mn	6 6	4.878 4.959	0.012 (7)	0.059 (35) 0.060 (35)	4.937 (35) 5.019 (35)	0.016 (4)

Table S4: EXAFS fit parameters for Li_2MnO_3 sample discharged to 2 V during the 1st cycle.

$S_0^2 = 0.76$

$\Delta E_0 = 2.6\,(1.3)$

Path	N_{degen}	R_{theory} (Å)	α_{fit}	ΔR (Å)	R_{fit} (Å)	σ^2_{fit} (Å^2)
Mn-O_{N-N}	4.3 (4)	1.904	-0.003 (3)	-0.006 (6)	1.898 (6)	0.0029 (8)
Mn-Mn	2	2.845	0.006 (3)	0.017 (9)	2.862 (9)	0.0081 (7)
	1	2.851		0.017 (9)	2.868 (9)	
Mn-O	2	3.513	-0.005 (6)	-0.018 (22)	3.495 (22)	0.007(3)
	2	3.515		-0.018 (22)	3.497 (22)	
	2	3.516		-0.018 (22)	3.498 (22)	
	2	3.686		-0.018 (22)	3.668 (22)	
Mn-O	2	4.388	0.005 (9)	0.022 (42)	4.410 (42)	0.011 (6)
	2	4.390		0.022 (42)	4.412 (42)	
	2	4.395		0.022 (42)	4.417 (42)	
	2	4.578		0.023 (42)	4.601 (42)	
	2	4.579		0.023 (42)	4.602 (42)	
	2	4.587		0.023 (42)	4.610 (42)	
	2	4.594		0.023 (42)	4.617 (42)	
	2	4.599		0.023 (42)	4.622 (42)	
	2	4.638		0.023 (42)	4.661 (42)	
	2	4.672		0.023 (42)	4.695 (42)	
	2	4.693		0.024 (42)	4.717 (42)	
	2	4.721		0.024 (42)	4.745 (42)	
Mn-Mn	4	4.929	0.001 (5)	0.005 (25)	4.934 (25)	0.011 (2)
	2	4.937		0.005 (25)	4.942 (25)	
	2	5.012		0.005 (25)	5.017 (25)	
	2	5.030		0.005 (25)	5.035 (25)	

Table S5: EXAFS fit parameters for Li_2MnO_3 sample charged to 5 V during the 33^{rd} cycle.

$S_0^2 = 0.76$

$\Delta E_0 = 3.0\,(1.0)$

$X_{eff} = 0.73\,(6)$

Path	N_{degen}	R_{theory} (Å)	α_{fit}	ΔR (Å)	R_{fit} (Å)	σ^2_{fit} (Å^2)
Mn-O_{N-N}	4.3	1.921	-0.013 (2)	-0.025 (4)	1.896 (4)	0.0035 (6)
Mn-Mn	6	2.816	0.023 (3)	0.065 (9)	2.881 (9)	0.012 (1)
Mn-O	6 2	3.409 3.661	0.010 (5)	0.034 (18) 0.037 (18)	3.443 (18) 3.698 (18)	0.006 (2)
Mn-O	12 12	4.422 4.619	0.003 (10)	0.013 (46) 0.014 (46)	4.435 (46) 4.633 (46)	0.013 (7)
Mn-Mn	6 6	4.878 4.959	0.015 (6)	0.073 (30) 0.074 (30)	4.951 (30) 5.033 (30)	0.017 (3)

Table S6: EXAFS fit parameters for Li_2MnO_3 sample discharged to 2 V during the 33^{rd} cycle.

$S_0^2 = 0.76$

$\Delta E_0 = -2.4\,(1.0)$

$X_{eff} = 0.61\,(5)$

Path	N_{degen}	R_{theory} (Å)	α_{fit}	ΔR (Å)	R_{fit} (Å)	σ^2_{fit} (Å^2)
Mn-O_{N-N}	4.3	1.904	-0.004 (2)	-0.008 (4)	1.896 (4)	0.0034 (7)
Mn-Mn	2	2.845	0.011 (4)	0.031 (12)	2.876 (12)	0.010(1)
	1	2.851		0.031 (12)	2.882 (12)	
Mn-O	2	3.513	-0.033 (4)	-0.116 (15)	3.397 (15)	0.003 (1)
	2	3.515		-0.116 (15)	3.399 (15)	
	2	3.516		-0.116 (15)	3.400 (15)	
	2	3.686		-0.122 (15)	3.564 (15)	
Mn-O	2	4.388	0.009 (5)	0.040 (24)	4.428 (24)	0.005 (2)
	2	4.390		0.040 (24)	4.430 (24)	
	2	4.395		0.040 (24)	4.435 (24)	
	2	4.578		0.041 (24)	4.619 (24)	
	2	4.579		0.041 (24)	4.620 (24)	
	2	4.587		0.041 (24)	4.628 (24)	
	2	4.594		0.041 (24)	4.635 (24)	
	2	4.599		0.041 (24)	4.640 (24)	
	2	4.638		0.042 (24)	4.680 (24)	
	2	4.672		0.042 (24)	4.714 (24)	
	2	4.693		0.042 (24)	4.735 (24)	
	2	4.721		0.043 (24)	4.763 (24)	
Mn-Mn	4	4.929	-0.005 (6)	-0.025 (30)	4.904 (30)	0.014(3)
	2	4.937		-0.025 (30)	4.912 (30)	
	2	5.012		-0.025 (30)	5.987 (30)	
	2	5.030		-0.025 (30)	5.005 (30)	

Table S7: Statistical EXAFS fit parameters for various Li_2MnO_3 samples. N_{idp} is the number of independent data points, N_{vary} is the number of fitting variables and ν is the number of degree of freedom ($\nu = N_{idp} - N_{vary}$)

Sample	Δk (Å^{-1})	ΔR (Å)	N_{idp}	N_{vary}	ν	χ^2	χ^2_ν	R
Pristine	3.9 - 13.5	1.0 - 5.1	24	12	12	732	59	0.008
5 V (1st cycle)	3.8 - 11.9	1.0 - 5.0	20	12	8	3177	378	0.013
2 V (1st cycle)	3.8 - 12.0	1.2 - 5.0	19	12	7	1667	221	0.011
5 V (33rd cycle)	3.8 - 11.8	1.0 - 5.0	20	12	8	93	12	0.010
2 V (33rd cycle)	3.8 - 11.8	1.0 - 5.0	20	12	8	80	10	0.011

Graphical TOC Entry